Interplay of magnetism and dimerization in the pressurized Kitaev material β-Li$_2$IrO$_3$

Bin Shen ⬤,[*] Anton Jesche, Maximilian L. Seidler, Friedrich Freund, Philipp Gegenwart ⬤,[†] and Alexander A. Tsirlin ⬤[‡]

Experimental Physics VI, Center for Electronic Correlations and Magnetism, University of Augsburg, 86159 Augsburg, Germany

We present magnetization measurements on polycrystalline β-Li$_2$IrO$_3$ under hydrostatic pressures up to 3 GPa and construct the temperature-pressure phase diagram of this material. Our data confirm that magnetic order breaks down in a first-order phase transition at $p_c \approx 1.4$ GPa and additionally reveal a steplike feature— magnetic signature of structural dimerization—that appears at p_c and shifts to higher temperatures upon further compression. Following the structural study by L. S. I. Veiga *et al.* [Phys. Rev. B **100**, 064104 (2019)], we suggest that a partially dimerized phase with a mixture of magnetic and nonmagnetic Ir^{4+} sites develops above p_c. This phase is thermodynamically stable between 1.7 and 2.7 GPa according to our *ab initio* calculations. It confines the magnetic Ir^{4+} sites to weakly coupled tetramers with a singlet ground state and no long-range magnetic order. Our results rule out the formation of a pressure-induced spin-liquid phase in β-Li$_2$IrO$_3$ and reveal peculiarities of the magnetism collapse transition in a Kitaev material. We also show that a compressive strain imposed by the pressure treatment of β-Li$_2$IrO$_3$ enhances signatures of the 100 K magnetic anomaly at ambient pressure.

I. INTRODUCTION

The Kitaev model is arguably one of the best settings for the experimental realization of quantum spin liquid in solid-state materials [1,2]. Recent efforts have resulted in the identification of several compounds with predominant Kitaev exchange [3], but all these compounds simultaneously showed long-range magnetic order caused by residual non-Kitaev interactions [4]. External pressure was considered as a convenient tuning parameter that may reduce unwanted interactions, suppress magnetic order, and bring a material closer to the Kitaev limit [5,6]. However, hydrostatic pressure experiments performed on several model compounds—different polymorphs of Li$_2$IrO$_3$ [7] and α-RuCl$_3$ [8–11]—all revealed a competing structural instability (dimerization) that shortens one third of the metal-metal distances on the (hyper)honeycomb spin lattice and eliminates local magnetism of the $4d/5d$ ions [12–15].

Among the model compounds tested under pressure, only β-Li$_2$IrO$_3$ with the hyperhoneycomb lattice of the Ir^{4+} ions and the Néel temperature of $T_N = 38$ K at ambient pressure [16–19] showed some promise of entering the spin-liquid state before structural dimerization occurred. Magnetization and muon spin relaxation (μSR) measurements revealed an abrupt suppression of magnetic order at $p_c \approx 1.4$ GPa, with a mixture of dynamic and randomly frozen spins above this pressure [20]. In contrast, the structural dimerization was observed only at $p_{dim} \simeq 4$ GPa at room temperature [14,20,21]. Taken together, these results were interpreted as the gradual tuning of magnetic interactions in β-Li$_2$IrO$_3$ toward a spin-liquid phase

that sets in above p_c, well before the structural transformation at p_{dim}. However, this putative spin-liquid phase must be rather fragile, as some of its spins become frozen below 15–20 K, presumably into a glassy state.

Subsequent low-temperature x-ray diffraction (XRD) experiments [22] challenged this scenario. The critical pressure p_{dim} was shown to decrease upon cooling, and below 50 K a structural transformation was observed at around p_c concomitant with the suppression of magnetic order. However, the transformation to the dimerized phase was not completed up to at least 2.0–2.5 GPa. At low temperatures, the phase composition right above p_c is either a mixture of the fully dimerized ($C2/c$) and nondimerized ($Fddd$) phases or a distinct partially dimerized ($P2_1/n$) phase [22] (see Fig. 1). Interestingly, the μSR experiments above p_c showed neither a dimerized state nor a pure spin-liquid state but, rather, a combination of frozen and dynamic spins [20] that could also be a result of multiple structural phases being present in the sample around this pressure. Moreover, no *magnetic* signatures of structural dimerization in β-Li$_2$IrO$_3$ have been reported until now.

Here, we shed light on some of these peculiarities using improved magnetization measurements under pressure. We show that a steplike feature in temperature-dependent magnetic susceptibility—the magnetic signature of structural dimerization—appears right above p_c. This feature confirms that the structural transformation not only accompanies, but also triggers the suppression of the long-range magnetic order in β-Li$_2$IrO$_3$. Our data exclude the presence of the nondimerized phase above p_c and corroborate the formation of the partially dimerized phase as the most plausible state at intermediate pressures. Using *ab initio* calculations we show that this phase is thermodynamically stable in a finite pressure range above p_c and features magnetic as well as nonmagnetic Ir^{4+} sites. The magnetic sites form weakly coupled

---

[*]bin.shen@uni-a.de
[†]philipp.gegenwart@uni-a.de
[‡]altsirlin@gmail.com

tetramers, which are expected to show cluster magnetism and naturally evade long-range magnetic order. Intriguingly, the low-temperature susceptibility of this partially dimerized phase also shows a Curie-like upturn with the paramagnetic effective moment of about $0.7\mu_B$ that persists far above p_c.

II. METHODS

The polycrystalline sample of β-Li$_2$IrO$_3$ was prepared by a solid-state reaction, as described in Ref. [20]. Sample quality was controlled by XRD (Rigaku MiniFlex; CuK$_\alpha$ radiation). Magnetization was measured using the MPMS3 SQUID magnetometer from Quantum Design. The powder sample was loaded into an opposed-anvil-type CuBe pressure cell. Measurement run Nos. 1 and 2 were carried out with a 1.8-mm anvil culet and a gasket with the sample space diameter of 0.9 mm. In this case, pressures up to 1.8 GPa could be reached. Higher pressures, up to 3.0 GPa, were achieved in run No. 3 with a 1-mm anvil culet and a gasket with the sample space diameter of 0.5 mm. Daphne oil 7373 was used as the pressure-transmitting medium. Pressure was determined by measuring the superconducting transition of a small piece of Pb. Magnetization of the empty cell was taken as the background.

Pressure was applied at room temperature. The cell was cooled down to 2 K, and the data were collected upon warming unless specified otherwise. Then the pressure was increased at room temperature, and the procedure was repeated until the highest pressure feasible with the current gasket was reached. Data on decompressed samples were also collected upon warming.

While this experimental procedure is very similar to the one implemented in Ref. [20], and the same pressure cell has been used for the measurement, we took special care with the background subtraction in order to measure the weak signal above p_c with a much higher accuracy than in our previous study. We developed software that allows point-by-point subtraction of the background signal and easy visual control of this procedure [23]. Moreover, the number of raw data points for each temperature point was increased to 400 with MPMS3, compared to 48 with the much older MPMS 5-T instrument used in Ref. [20].

High-resolution XRD data [24] were collected on a pristine powder sample of β-Li$_2$IrO$_3$ and on the samples recovered after decompression from run Nos. 1 and 2. XRD measurements were performed at room temperature at the ID22 beamline of the European Synchrotron Radiation Facility (ESRF; Grenoble) using the wavelength of 0.3542 Å and 13 scintillation detectors, each preceded by a Si(111) analyzer crystal. The samples were placed in thin-walled glass capillaries and spun during the measurement. Rietveld refinements were performed using the JANA2006 software [25].

Full-relativistic density-functional-theory (DFT) band-structure calculations were used to assess the thermodynamic stability of pressure-induced phases and their magnetism. Structural relaxations were performed in VASP [26,27] with the Perdew-Burke-Ernzerhof (PBE) for solids (PBEsol) exchange-correlation potential [28], which yields the best agreement with the equilibrium unit cell volume of β-Li$_2$IrO$_3$ at ambient pressure. Correlation effects were taken into
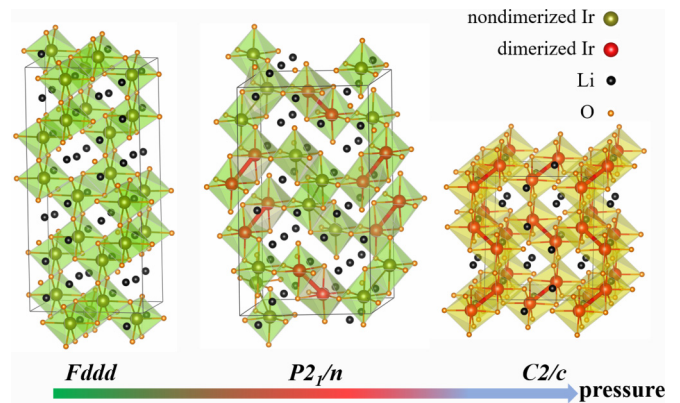

FIG. 1. Nondimerized ($Fddd$), partially dimerized ($P2_1/n$), and fully dimerized ($C2/c$) phases of β-Li$_2$IrO$_3$ under pressure, with the crystal structures taken from Ref. [22]. Red Ir–Ir bonds denote the dimerized Ir^{4+} ions.

account on the DFT+U + SO level with the on-site Coulomb repulsion parameter $U_d = 1.0$ eV and Hund's coupling $J_d = 0.3$ eV. Additionally, FPLO calculations [29] were performed on the PBE level to obtain the density of states as well as tight-binding parameters via Wannier projections.

III. EXPERIMENTAL RESULTS

A. Pressure evolution

Figure 2 shows the magnetic susceptibility χ as a function of the temperature measured under various pressures. Below 1.4 GPa, $\chi(T)$ increases smoothly upon cooling from room temperature, followed by a sharp upturn around 50 K and an anomaly at $T_N \approx 38$ K due to the magnetic ordering transition. The value of T_N is nearly independent of the applied pressure. From the Ehrenfest relation for the specific heat and thermal expansion one estimates the initial pressure dependence of $(dT_N/dp)_{p\to0} = 0.7$ K/GPa [20], so we expect only a marginal increase in T_N upon compression.

In the narrow pressure range between 1.4 and 1.5 GPa, the transition at T_N can still be observed, but absolute values of the susceptibility become much lower. The transition coexists with a steplike feature appearing at 120–150 K. This feature is accompanied by a narrow thermal hysteresis [Fig. 2(b)] and strongly resembles the magnetic signature of structural dimerization in α-RuCl$_3$ [8,10].

At even higher pressures, only the dimerization anomaly can be observed. It shifts to higher temperatures with increasing pressure [Figs. 2(b), 2(d), and 2(f)], while below this anomaly the susceptibility becomes nearly temperature independent, except below 50 K, where a Curie-like upturn appears. All these features were systematically observed in three separate measurement runs and are thus well reproducible. In run No. 3, we used a smaller gasket and reached the pressure of 3 GPa, at which the dimerization temperature T_d becomes as high as 250 K, whereas the Curie-like upturn remains nearly unchanged [Fig. 2(f)]. The slightly negative value of the susceptibility at high temperatures for run No. 3 [Fig. 2(f)] is likely due to an imperfect background subtraction caused by the more severe deformation of the gasket, since the
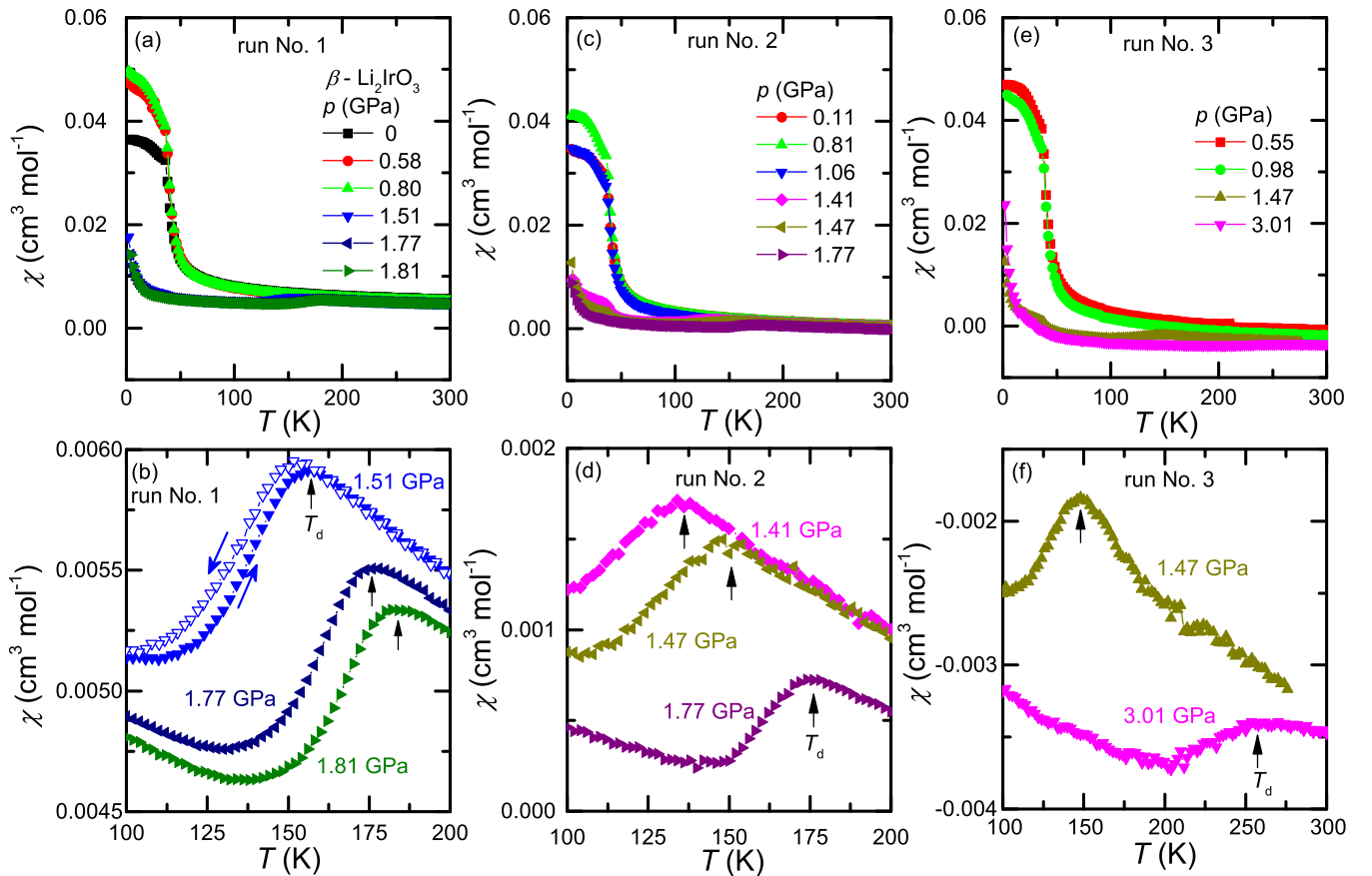
FIG. 2. Temperature-dependent magnetic susceptibility $\chi(T)$ of β-Li$_2$IrO$_3$ measured under various pressures from 2 to 300 K in the 1 T magnetic field. (a), (c), (e) Data from three different runs. (b), (d), (f) Magnifications of the steplike features due to the dimerization transition at T_d shown by the black arrows. A hysteresis loop is clearly seen at 1.51 GPa in (b) upon cooling and warming.

sample volume and, thus, intrinsic magnetic signal are much reduced compared to those in run Nos. 1 and 2.

For the Curie-Weiss analysis, we use the temperature range below 30 K [Fig. 3(a)] to avoid contributions from the paramagnetic spins of the nondimerized phase. The fit with $\chi = \chi_0 + C/(T - \theta_{CW})$ (χ_0, a residual temperature-independent term; C, the Curie constant; θ_{CW}, the Curie-Weiss temperature) returns the effective moment of about $0.7\mu_B$/f.u. and the Curie-Weiss temperature $\theta_{CW} \simeq -2$ K, both reproducible between the different measurement runs and nearly pressure independent [Fig. 3(b)]. The very small θ_{CW} indicates nearly decoupled magnetic moments, which are reminiscent of impurity spins. For comparison, the Curie-Weiss fit of the ambient-pressure data between 200 and 300 K returns the effective moment of $1.79\mu_B$/f.u., in good agreement with the expected value of $1.73\mu_B$ for the $j_{eff} = \frac{1}{2}$ state of Ir^{4+}. Using $(0.7/1.79)^2 = 0.152$, we estimate that roughly 15% of the Ir atoms should be responsible for the Curie tail observed at low temperatures above p_c. However, this fraction may also be lower because x-ray absorption data show a rapid departure from the $j_{eff} = \frac{1}{2}$ state with increasing pressure [30].

With these revised magnetization data, we are able to confirm our earlier conclusion [20] that the magnetic order in β-Li$_2$IrO$_3$ is suppressed around 1.4 GPa upon a first-order pressure-induced phase transition. However, this transition

clearly has a structural component that leads to at least a partial dimerization with a fraction of the Ir^{4+} ions paired into dimers, wherein their magnetic response is fully suppressed above p_c and below T_d. Low-temperature XRD data [22] suggest two possible scenarios for the phase composition above p_c: (i) a mixture of the fully dimerized and nondimerized phases and (ii) a partially dimerized phase. Our results exclude the former and clearly support the latter, because the nondimerized phase with its $T_N \simeq 38$ K should appear prominently in the magnetic susceptibility data. However, no signatures of T_N are seen above 1.51 GPa [Fig. 3(a)]. In the narrow pressure range from 1.41 to 1.51 GPa, a kink in the susceptibility is still observed because of the phase coexistence at the first-order phase transition.

The temperature-pressure phase diagram inferred from the susceptibility data (Fig. 4) shows strong similarities to that of α-RuCl$_3$ [8]. The long-range-ordered phase is robust below the critical pressure p_c. At p_c, this phase abruptly disappears and gives way to a high-pressure phase characterized by structural dimerization with a strong pressure dependence of T_d.

Notwithstanding these apparent similarities to α-RuCl$_3$, it seems premature to associate the high-pressure phase of β-Li$_2$IrO$_3$ with the fully dimerized ($C2/c$) state that has been observed above 4 GPa at room temperature [14,20]. Low-temperature XRD excludes a full transformation into the $C2/c$
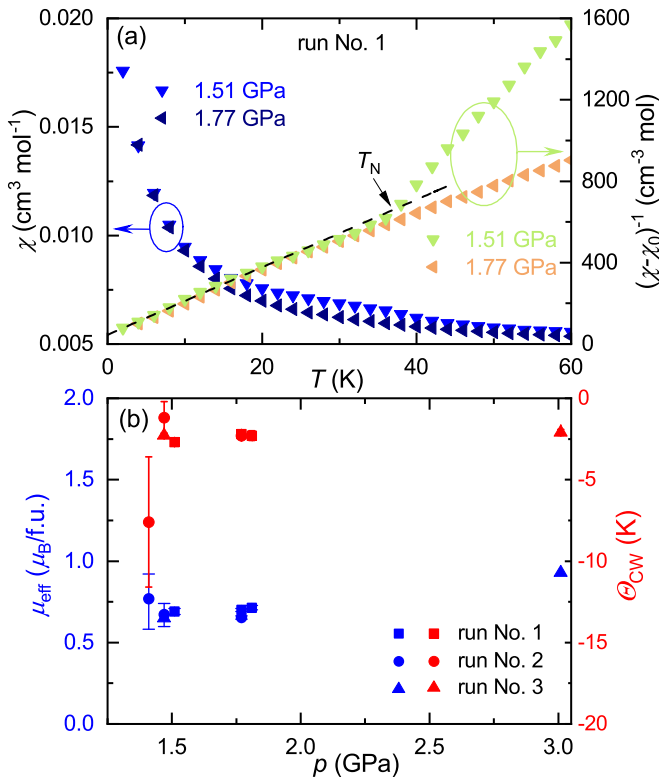
FIG. 3. Curie-Weiss analysis of the susceptibility data. (a) Magnetic susceptibility χ and inverse susceptibility $(\chi - \chi_0)^{-1}$ measured at 1.51 and 1.77 GPa in run No. 1. The dashed line shows the Curie-Weiss fitting at 1.51 GPa. (b) The paramagnetic effective moment and Curie-Weiss temperature θ_{CW} extracted from the Curie-Weiss fits for the low-temperature part of the magnetic susceptibility.

phase already at p_c. Moreover, the μSR observations do not support a purely nonmagnetic phase above p_c and suggest a partial spin freezing below 15–20 K [20].

These μSR signatures of spin freezing should be taken with caution, though, as soon as dimerization comes into play. Freezing effects are sometimes observed in μSR experiments on dimer magnets [31–33], presumably because muons perturb spin dimers and alter their singlet ground state. In this case, spin freezing is seen as the increase in the volume fraction of static spins in μSR but does not appear in the magnetic susceptibility. A similar situation occurs in β-Li$_2$IrO$_3$ (Fig. 5). Magnetic susceptibility measured at 1.77 GPa with $\mu_0 H = 0.1$ T, the lowest field that allows a reliable measurement of the weak signal in the pressure cell, does not show a splitting of the field-cooled and zero-field-cooled data around 15–20 K, the temperature range where the volume fraction of static spins increases according to μSR [20]. Therefore, spin-freezing effects in the high-pressure phase of β-Li$_2$IrO$_3$ seem to be extrinsic and driven by muons.

B. After decompression

In Fig. 6(b), we compare the 1 T magnetic susceptibility of the pristine β-Li$_2$IrO$_3$ sample and the samples retrieved from run Nos. 1 and 2 after decompression. Surprisingly, the anomaly at around 100 K appears after decompression. This anomaly was also present in the pristine sample, but in much
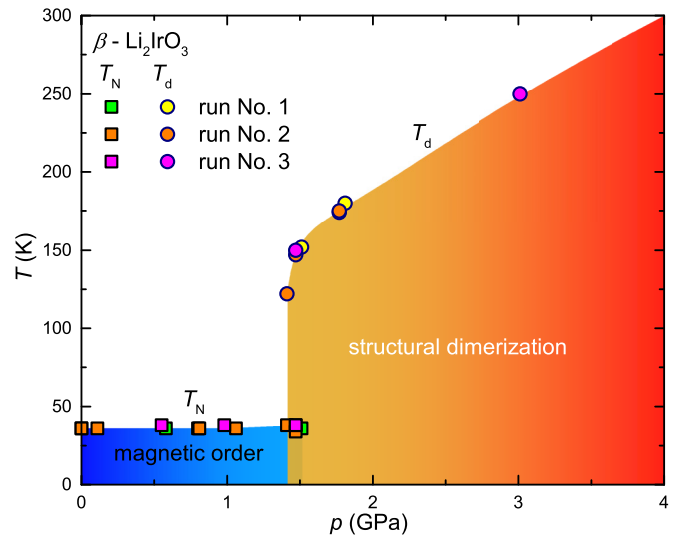
lower magnetic fields only [Fig. 6(a)]. It strongly resembles the "high-temperature" magnetic anomaly reported by Ruiz *et al.* [34], who argued its intrinsic nature and a possible relation to spin-orbital magnetic species. Their data suggest that this anomaly is very sensitive to the applied magnetic field and should be fully suppressed in a field of 1 T. This is indeed the case in our pristine sample but not in the decompressed ones, where the anomaly remains clearly visible even at 1 T.

To assess structural changes introduced by the pressure treatment, we inspected the decompressed samples using high-resolution powder XRD. Rietveld refinement did not reveal any differences in the atomic positions between decom-
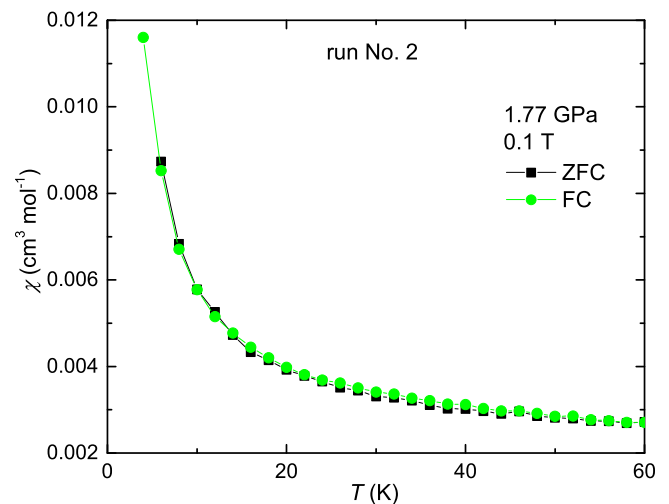

FIG. 4. Temperature-pressure phase diagram of β-Li$_2$IrO$_3$ inferred from the magnetic susceptibility data. T_N marks the antiferromagnetic transition temperature of the nondimerized phase, whereas T_d stands for the dimerization transition temperature of the high-pressure phase.

FIG. 5. Zero-field-cooled and field-cooled magnetic susceptibility of β-Li$_2$IrO$_3$ measured at 1.77 GPa in the applied field of 0.1 T (run No. 2). No FC/ZFC splitting is observed around 15–20 K where the volume fraction of static spins increases according to μSR [20].
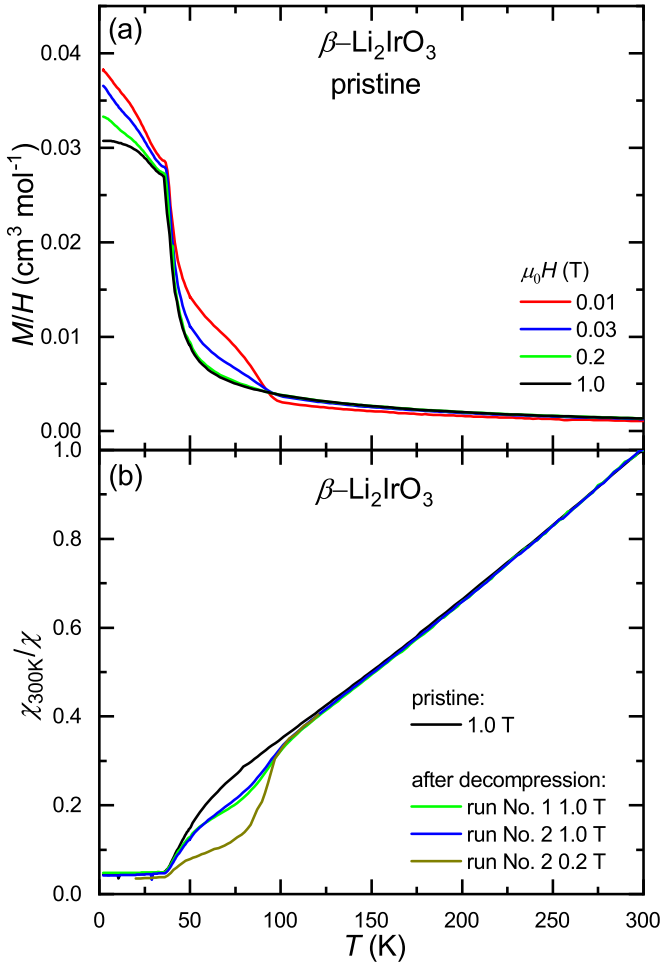
FIG. 6. (a) Temperature-dependent magnetic susceptibility $\chi(T)$ of pristine β-Li_2IrO_3 measured upon cooling in various magnetic fields. Note that the 100 K anomaly observed in low fields is fully suppressed already at 0.2 T. (b) Normalized inverse magnetic susceptibility of pristine β-Li_2IrO_3, samples of run No. 1 after decompression, and samples of run No. 2 after decompression, respectively.

pressed and pristine samples of β-Li_2IrO_3. However, a careful comparison of the lattice and profile parameters (Table I) indicated a slight increase in the reflection width gauged by the profile parameter LY and, more drastically, a systematic reduction in the lattice parameters, especially in a and in b. This change corresponds to a small compressive strain that is

TABLE I. Lattice parameters a, b, and c and the Lorentzian profile parameter LY extracted from high-resolution powder XRD data collected on pristine and decompressed samples of β-Li_2IrO_3. Error bars are from the Rietveld refinement. The pristine sample was synthesized as powder and shows slightly different lattice parameters compared to Ref. [19], where a crushed single crystal was used.

	a (Å)	b (Å)	c (Å)	LY (10^{-2} deg)
Pristine	5.91191(2)	8.46414(2)	17.8183(1)	10.33(2)
Run No. 1	5.90737(2)	8.45852(2)	17.8133(1)	11.18(2)
Run No. 2	5.91016(2)	8.46208(2)	17.8173(1)	11.44(2)

TABLE II. Fitted parameters of the second-order Murnaghan equation of state for different phases of β-Li_2IrO_3. Energies E_0 are given relative to the energy minimum of the nondimerized $Fddd$ phase.

Space group	E_0 (meV/f.u.)	V_0 (Å³/f.u.)	B_0 (GPa)	B_0'
$Fddd$	0	55.48(3)	103(3)	4.7(4)
$C2/c$	18(1)	54.11(2)	114(2)	5.9(3)
$P2_1/n$	100(1)	54.91(3)	101(3)	6.1(3)

more pronounced in the run No. 1 sample. Indeed, this sample showed a larger magnitude of the 100 K magnetic anomaly. While the exact origin of this anomaly remains unknown and requires a further dedicated study, we have shown that the anomaly can be enhanced by a compressive strain that, on the other hand, has no influence on T_N. This indicates that long-range magnetic order in β-Li_2IrO_3 is by far more robust and less sensitive to perturbations than the elusive magnetic anomaly at 100 K.

We also note that the strain in the decompressed samples may be caused by a slight deviation from the ideal hydrostatic conditions during the pressure treatment. Nevertheless, we observe an excellent match between the magnetization data collected during run Nos. 1 and 2 despite the different amount of compressive strain accumulated in these two samples. This indicates that no main features of the pressure-induced behavior—the breakdown of magnetic order at p_c and the structural dimerization above p_c—are affected by this minor deviation from the hydrosticity.

IV. *AB INITIO* MODELING

A. Phase stability

We now extend this analysis with the *ab initio* modeling for the partially dimerized phase ($P2_1/n$) as a plausible candidate state for β-Li_2IrO_3 above p_c. The XRD data in Ref. [22] reported this phase at 50 K, whereas at 25 K it could not be uniquely distinguished from a mixture of the nondimerized ($Fddd$) and fully dimerized ($C2/c$) phases. Therefore, the first question regarding the partially dimerized phase is its thermodynamic stability. Should there be a pressure range where it is more stable than both the $Fddd$ and the $C2/c$ phases, one may expect this partially dimerized phase to appear upon compression before full dimerization occurs.

In the following, we compare total energies and enthalpies of the phases in question. Crystal structures are relaxed at a fixed volume to obtain the volume dependence of the energy, which is fitted with the Murnaghan equation of state,

$$E(V) = E_0 + B_0 V_0 \left[\frac{1}{B_0'(B_0' - 1)} \left(\frac{V}{V_0} \right)^{1-B_0'} + \frac{1}{B_0'} \frac{V}{V_0} - \frac{1}{B_0' - 1} \right].$$

The fit returns the equilibrium energy (E_0), equilibrium volume (V_0), and bulk modulus (B_0) and its pressure derivative (B_0'), as listed in Table II.
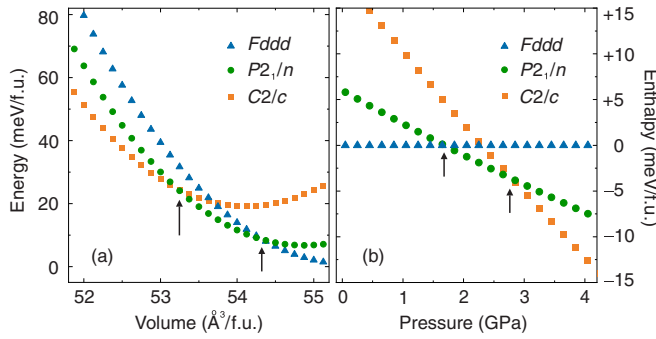
FIG. 7. Comparison of the nondimerized ($Fddd$), partially dimerized ($P2_1/n$), and fully dimerized ($C2/c$) phases: (a) volume dependence of energy; (b) pressure dependence of enthalpy.

Figure 7 shows that the fully and partially dimerized phases are indeed stabilized under pressure. The fully dimerized phase sets in around 2.7 GPa, preceded by the partially dimerized phase, which becomes thermodynamically stable already at 1.7 GPa. These transition pressures are in very good agreement with the experimental values of, respectively, 1.5 and 2.3 GPa at 50 K, as determined from the XRD data [22]. Our *ab initio* results thus support the partially dimerized phase as a thermodynamically stable form of β-Li$_2$IrO$_3$ at intermediate pressures. It may indeed appear upon compressing β-Li$_2$IrO$_3$ at low temperatures.

B. Magnetism

We now analyze the magnetism of this partially dimerized phase. A simple inspection of the crystal structure suggests that half of the Ir^{4+} ions—those with the Ir–Ir distance of 2.66 Å (Ir2 and Ir4 in the notation of Ref. [22])—should be nonmagnetic, while the remaining half (Ir1 and Ir3 with the Ir–Ir distance of 2.92 Å) should remain magnetic akin to the parent undimerized phase. Indeed, in DFT+U+SO calculations we find magnetic moments of about $0.4\mu_B$ in the nondimerized phase, no moment in the dimerized phase, and the drastically different moments of $0.05\mu_B$ on Ir2 and Ir4 vs $0.35\mu_B$ on Ir1 and Ir3 in the partially dimerized phase.

This conclusion is additionally supported by the structure of the Ir t_{2g} bands calculated on the DFT+SO level without taking electronic correlations into account, such that no bandgap opens at the Fermi level (Fig. 8). In the nondimerized phase, the splitting between the bands below and above -0.5 eV reflects the separation of the atomic states into $j_{\text{eff}} = \frac{3}{2}$ and $j_{\text{eff}} = \frac{1}{2}$, respectively. This splitting disappears in the dimerized phase, where one finds instead several narrow bands arising from molecular orbitals of the Ir$_2$ dimers, similarly to Refs. [35] and [36]. The partially dimerized phase combines both features. The Ir2 and Ir4 states participate in the dimer formation and, therefore, provide dominant contributions to the upper and lower bands around 0.3 and -1.8 eV, respectively. The Ir1 and Ir3 states span a comparatively narrower energy range between -1.2 and 0.1 eV only.

Partial dimerization breaks the hyperhoneycomb lattice of β-Li$_2$IrO$_3$ into finite Ir1–Ir3–Ir3–Ir1 clusters with the X-Y-X Kitaev bonds (Fig. 9). The Z-type bonds disappear because they always involve either Ir2 or Ir4. The nature of exchange
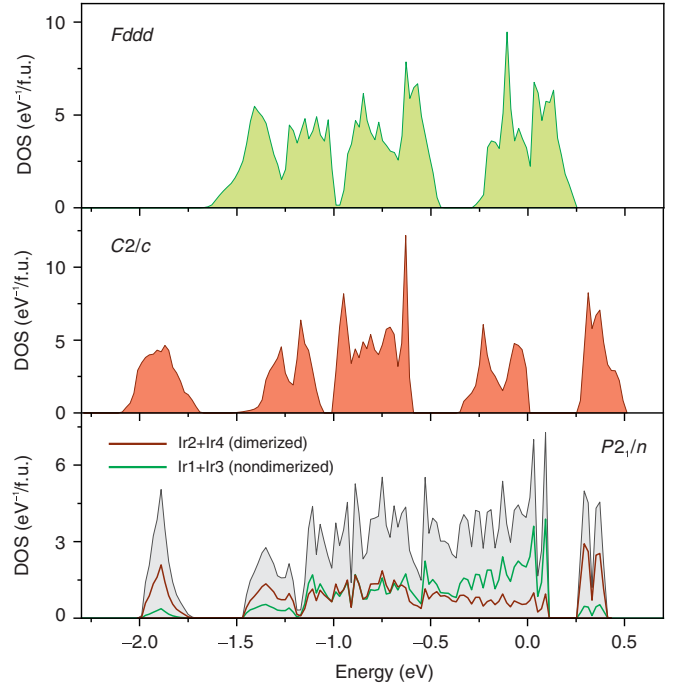

FIG. 8. Density of states corresponding to the Ir t_{2g} bands in the three phases of β-Li$_2$IrO$_3$. Note that the partially dimerized phase ($P2_1/n$) shares features of both dimerized and nondimerized phases. The calculations are performed on the DFT+SO level without taking Coulomb correlations into account.

interactions is verified by a direct calculation of the exchange parameters of the spin Hamiltonian,

$$\mathcal{H} = \sum_{\langle ij \rangle} J_{ij} \mathbf{S}_i \mathbf{S}_j + \sum_{\langle ij \rangle} K_{ij} S_i^\gamma S_j^\gamma + \sum_{\langle ij \rangle} \Gamma_{ij} \left(S_i^\alpha S_j^\beta + S_i^\beta S_j^\alpha \right),$$

where J_{ij}, K_{ij}, and Γ_{ij} stand, respectively, for the Heisenberg exchange, Kitaev exchange, and off-diagonal anisotropy, and $\alpha \neq \beta \neq \gamma$ ($\gamma = X$ for Ir1–Ir3 and $\gamma = Y$ for Ir3–Ir3). These parameters are obtained from the superexchange theory developed in Refs. [37] and [38] following the procedure described in Ref. [20].

We find $J_{13} = -6.3$ meV, $K_{13} = -14.5$ meV, and $\Gamma_{13} = -18.9$ meV for the Ir1–Ir3 bonds, as well as $J_{33} = -4.4$ meV, $K_{33} = -9.9$ meV, and $\Gamma_{33} = -11.9$ meV for the Ir3–Ir3
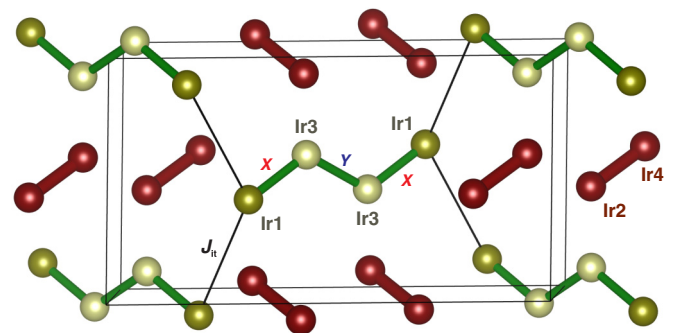

FIG. 9. Partially dimerized phase of β-Li$_2$IrO$_3$ with nonmagnetic Ir2–Ir4 dimers and magnetic Ir1–Ir3–Ir3–Ir1 tetramers. J_{it} is the coupling between the tetramers.

bonds. These parameters are only marginally different from the ambient-pressure values obtained using the same superexchange theory ($K = -12.1$ meV, $\Gamma = -13.5$ meV, and $J = -4.8$ meV [20]). Experimentally, one finds $|K| \simeq |\Gamma| \simeq 13$ meV [19,39] and $J \simeq 0.3$ meV [40]. Exact diagonalization for the Ir1–Ir3–Ir3–Ir1 tetramer was performed in Mathematica using exchange parameters for the partially dimerized phase. The energy spectrum of the tetramer features a singlet ground state separated from the first excited state by $\Delta \simeq 9.1$ meV. For comparison, we also applied experimental exchange parameters at ambient pressure to the tetramer and arrived at a quite similar low-energy spectrum with $\Delta \simeq 8.5$ meV.

We thus expect that the partially dimerized phase of β-Li$_2$IrO$_3$ is magnetic, but no long-range order ensues because tetramers remain decoupled. Their singlet state is protected by the sizable gap Δ. This result is consistent with our experimental observation that magnetic order vanishes above p_c, but signatures of local magnetism remain visible also at higher pressures.

The couplings between the tetramers are mediated by the nonmagnetic Ir2–Ir4 dimers. The shortest superexchange pathway, with the Ir1–Ir1 distance of 5.10 Å, yields a coupling with $J_{it} = -0.3$ meV, $K_{it} = -0.8$ meV, and $\Gamma_{it} = 0.1$ meV (Fig. 9). This weak coupling is by far insufficient to close the gap Δ and induce long-range order.

V. DISCUSSION AND SUMMARY

Our data call into question the earlier scenario of pressure-induced spin-liquid formation in β-Li$_2$IrO$_3$ [20]. We have shown that the breakdown of magnetic order at p_c leads to a steplike feature in the magnetic susceptibility: a hallmark of structural dimerization. A small fraction of the nondimerized phase persists up to 1.5 GPa due to the pressure hysteresis of the first-order phase transition, but at higher pressures the magnetically ordered nondimerized phase vanishes entirely.

This leaves two possibilities for the low-temperature behavior of β-Li$_2$IrO$_3$ at pressures above p_c. One scenario is the fully dimerized state, similar to the high-pressure phase of α-RuCl$_3$, but with a significant number of defects that should account for the Curie-like upturn in the magnetic susceptibility at low temperatures. However, such a fully dimerized phase is at odds with the low-temperature XRD data at pressures right above p_c [22] and also fails to explain the μSR observation of mixed frozen and dynamic spins in the high-pressure phase. An interpretation of the μSR data would require that some of the muons break the singlet state of the dimers, thus causing spin freezing, while other muons leave dimers intact and observe dynamic spins. Importantly, the magnetic field distribution produced by these dynamic spins is temperature dependent and becomes broader below 40 K [20]. This fact would be especially difficult to reconcile with the scenario of complete dimerization.

The alternative scenario of the partially dimerized phase seems more promising. An important aspect of this phase is that its magnetic Ir^{4+} sites are confined to weakly coupled tetramer units and, therefore, evade magnetic ordering. The

spins of the tetramer remain dynamic down to zero temperature, but they form a cluster magnet rather than a genuine spin liquid. The separation of the Ir^{4+} ions into magnetic and nonmagnetic *within* one phase gives a natural explanation for the mixed μSR response of the dynamic and frozen spins coexisting in the sample. The frozen spins can be assigned to the nonmagnetic Ir^{4+} ions, with corresponding spin dimers perturbed by muons. The dynamic spins can be associated with the tetramers, and the temperature-dependent field distribution probed by muons may be caused by the development of spin-spin correlations on the tetramers. The 40:60 ratio of the static and dynamic spins in μSR seems rather close to the 50:50 ratio of the magnetic and nonmagnetic Ir^{4+} sites in the crystal structure, although some misbalance in the muon stop sites should probably be taken into account.

One aspect of our data that even the partially dimerized phase fails to explain is the Curie-like susceptibility upturn, which is not expected in the tetramers because their ground state is a singlet. It is then natural to ascribe this Curie-like upturn to impurity spins, even if no such upturn is observed at ambient pressure or at any pressure below p_c. Indeed, at ambient pressure the rapidly increasing magnetic susceptibility below T_N can mask the impurity signal or, alternatively, the impurities may become quenched when internal fields develop in the long-range-ordered state of β-Li$_2$IrO$_3$. It is also noteworthy that additional defects may be introduced by pressure treatment as compressive strain accumulates in the sample. Strain effects on the magnetism of β-Li$_2$IrO$_3$ are clearly an interesting venue for future studies. Intriguingly, the enigmatic 100 K magnetic anomaly appears to be sensitive to the strain.

Yet another aspect that requires further investigation is the transformation of the partially dimerized phase into the
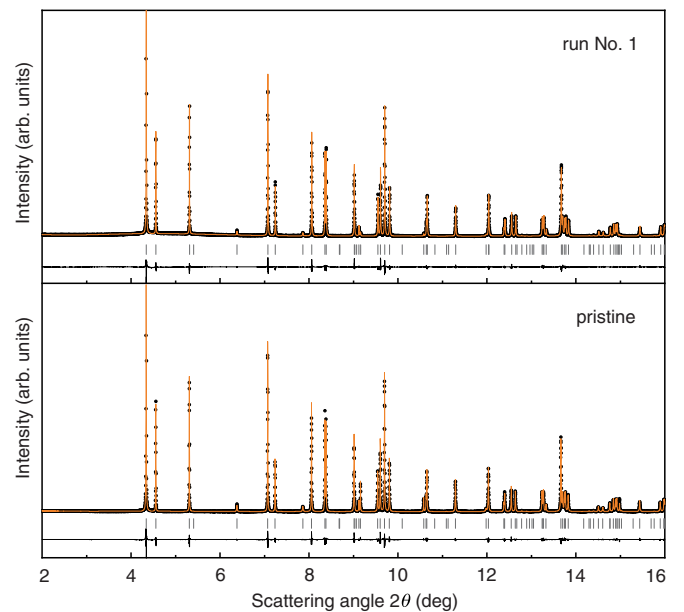

FIG. 10. Rietveld refinements versus high-resolution XRD data. Tick marks show reflection positions for the $Fddd$ structure of nondimerized β-Li$_2$IrO$_3$. The refinement residuals are $R_I = 0.028$ and $R_p = 0.067$ for the sample from run No. 1 and $R_I = 0.018$ and $R_p = 0.080$ for the pristine sample.

fully dimerized one. Our susceptibility data do not show any additional phase boundaries in the temperature-pressure phase diagram, but technical limitations restrict the highest pressure of our present study to 3 GPa, and already above 2 GPa the sensitivity of the measurement is reduced because of the smaller sample size. Magnetization measurements at higher pressures, as well as local probes, would certainly be useful to track further evolution of the unusual high-pressure phase of β-Li$_2$IrO$_3$.

In summary, we have revised the temperature-pressure phase diagram of β-Li$_2$IrO$_3$ using improved magnetization measurements. The breakdown of the long-range magnetic order around $p_c \simeq 1.4$ GPa is accompanied by the appearance of a steplike anomaly due to the structural dimerization. This observation rules out the scenario of pressure-induced spin liquid in this material and suggests a structural instability as the main cause for the breakdown of magnetic order. The high-pressure phase above p_c can be understood as a partially

dimerized phase with coexisting magnetic (nondimerized) and nonmagnetic (dimerized) Ir^{4+} sites.

APPENDIX: SAMPLE CHARACTERIZATION

In Fig. 10, we show Rietveld refinements for the pristine sample and the sample recovered after decompression from run No. 1. Both samples are well described by the $Fddd$ space group of β-Li$_2$IrO$_3$, albeit with a small difference in their lattice and profile parameters (Table I).

[1] M. Hermanns, I. Kimchi, and J. Knolle, Physics of the Kitaev model: Fractionalization, dynamic correlations, and material connections, Annu. Rev. Condens. Matter Phys. **9**, 17 (2018).

[2] H. Takagi, T. Takayama, G. Jackeli, G. Khaliullin, and S. E. Nagler, Concept and realization of Kitaev quantum spin liquids, Nat. Rev. Phys. **1**, 264 (2019).

[3] G. Jackeli and G. Khaliullin, Mott Insulators in the Strong Spin-Orbit Coupling Limit: From Heisenberg to a Quantum Compass and Kitaev Models, Phys. Rev. Lett. **102**, 017205 (2009).

[4] S. M. Winter, A. A. Tsirlin, M. Daghofer, J. van den Brink, Y. Singh, P. Gegenwart, and R. Valentí, Models and materials for generalized Kitaev magnetism, J. Phys.: Condens. Matter **29**, 493002 (2017).

[5] H.-S. Kim, Y. B. Kim, and H.-Y. Kee, Revealing frustrated local moment model for pressurized hyperhoneycomb iridate: Paving the way toward a quantum spin liquid, Phys. Rev. B **94**, 245127 (2016).

[6] R. Yadav, S. Rachel, L. Hozoi, J. van den Brink, and G. Jackeli, Strain- and pressure-tuned magnetic interactions in honeycomb Kitaev materials, Phys. Rev. B **98**, 121107(R) (2018).

[7] A. A. Tsirlin and P. Gegenwart, Kitaev magnetism through the prism of lithium iridate, Phys. Status Solidi B, 2100146 (2021).

[8] G. Bastien, G. Garbarino, R. Yadav, F. J. Martinez-Casado, R. Beltrán Rodríguez, Q. Stahl, M. Kusch, S. P. Limandri, R. Ray, P. Lampen-Kelley, D. G. Mandrus, S. E. Nagler, M. Roslova, A. Isaeva, T. Doert, L. Hozoi, A. U. B. Wolter, B. Büchner, J. Geck, and J. van den Brink, Pressure-induced dimerization and valence bond crystal formation in the Kitaev-Heisenberg magnet α-RuCl$_3$, Phys. Rev. B **97**, 241108(R) (2018).

[9] T. Biesner, S. Biswas, W. Li, Y. Saito, A. Pustogow, M. Altmeyer, A. U. B. Wolter, B. Büchner, M. Roslova, T. Doert, S. M. Winter, R. Valentí, and M. Dressel, Detuning the honeycomb of α-RuCl$_3$: Pressure-dependent optical studies reveal broken symmetry, Phys. Rev. B **97**, 220401(R) (2018).

[10] Y. Cui, J. Zheng, K. Ran, J. Wen, Z.-X. Liu, B. Liu, W. Guo, and W. Yu, High-pressure magnetization and NMR studies of α-RuCl$_3$, Phys. Rev. B **96**, 205147 (2017).

[11] G. Li, X. Chen, Y. Gan, F. Li, M. Yan, F. Ye, S. Pei, Y. Zhang, L. Wang, H. Su, J. Dai, Y. Chen, Y. Shi, X.-W. Wang,

L. Zhang, S. Wang, D. Yu, F. Ye, J.-W. Mei, and M. Huang, Raman spectroscopy evidence for dimerization and Mott collapse in α-RuCl$_3$ under pressures, Phys. Rev. Mater. **3**, 023601 (2019).

[12] V. Hermann, M. Altmeyer, J. Ebad-Allah, F. Freund, A. Jesche, A. A. Tsirlin, M. Hanfland, P. Gegenwart, I. I. Mazin, D. I. Khomskii, R. Valentí, and C. A. Kuntscher, Competition between spin-orbit coupling, magnetism, and dimerization in the honeycomb iridates: α-Li$_2$IrO$_3$ under pressure, Phys. Rev. B **97**, 020104(R) (2018).

[13] J. P. Clancy, H. Gretarsson, J. A. Sears, Y. Singh, S. Desgreniers, K. Mehlawat, S. Layek, G. Kh. Rozenberg, Y. Ding, M. H. Upton, D. Casa, N. Chen, J. Im, Y. Lee, R. Yadav, L. Hozoi, D. Efremov, J. van den Brink, and Y.-J. Kim, Pressure-driven collapse of the relativistic electronic ground state in a honeycomb iridate, npj Quantum Mater. **3**, 35 (2018).

[14] T. Takayama, A. Krajewska, A. S. Gibbs, A. N. Yaresko, H. Ishii, H. Yamaoka, K. Ishii, N. Hiraoka, N. P. Funnell, C. L. Bull, and H. Takagi, Pressure-induced collapse of the spin-orbital Mott state in the hyperhoneycomb iridate β-Li$_2$IrO$_3$, Phys. Rev. B **99**, 125127 (2019).

[15] V. Hermann, J. Ebad-Allah, F. Freund, A. Jesche, A. A. Tsirlin, P. Gegenwart, and C. A. Kuntscher, Optical signature of the pressure-induced dimerization in the honeycomb iridate α-Li$_2$IrO$_3$, Phys. Rev. B **99**, 235116 (2019).

[16] A. Biffin, R. D. Johnson, Sungkyun Choi, F. Freund, S. Manni, A. Bombardi, P. Manuel, P. Gegenwart, and R. Coldea, Unconventional magnetic order on the hyperhoneycomb Kitaev lattice in β-Li$_2$IrO$_3$: Full solution via magnetic resonant x-ray diffraction, Phys. Rev. B **90**, 205116 (2014).

[17] T. Takayama, A. Kato, R. Dinnebier, J. Nuss, H. Kono, L. S. I. Veiga, G. Fabbris, D. Haskel, and H. Takagi, Hyperhoneycomb Iridate β-Li$_2$IrO$_3$ as a Platform for Kitaev Magnetism, Phys. Rev. Lett. **114**, 077202 (2015).

[18] A. Ruiz, A. Frano, N. P. Breznay, I. Kimchi, T. Helm, I. Oswald, J. Y. Chan, R. J. Birgeneau, Z. Islam, and J. G. Analytis, Correlated states in β-Li$_2$IrO$_3$ driven by applied magnetic fields, Nat. Commun. **8**, 961 (2017).

[19] M. Majumder, F. Freund, T. Dey, M. Prinz-Zwick, N. Büttgen, Y. Skourski, A. Jesche, A. A. Tsirlin, and P. Gegenwart, Anisotropic temperature-field phase diagram of single crystalline β-Li$_2$IrO$_3$: Magnetization, specific heat, and ^{7}Li NMR study, Phys. Rev. Mater. **3**, 074408 (2019).

[20] M. Majumder, R. S. Manna, G. Simutis, J. C. Orain, T. Dey, F. Freund, A. Jesche, R. Khasanov, P. K. Biswas, E. Bykova, N. Dubrovinskaia, L. S. Dubrovinsky, R. Yadav, L. Hozoi, S. Nishimoto, A. A. Tsirlin, and P. Gegenwart, Breakdown of Magnetic Order in the Pressurized Kitaev Iridate β-Li$_2$IrO$_3$, Phys. Rev. Lett. **120**, 237202 (2018).

[21] S. Choi, H.-S. Kim, H.-H. Kim, A. Krajewska, G. Kim, M. Minola, T. Takayama, H. Takagi, K. Haule, D. Vanderbilt, and B. Keimer, Lattice dynamics and structural transition of the hyperhoneycomb iridate β-Li$_2$IrO$_3$ investigated by high-pressure Raman scattering, Phys. Rev. B **101**, 054102 (2020).

[22] L. S. I. Veiga, K. Glazyrin, G. Fabbris, C. D. Dashwood, J. G. Vale, H. Park, M. Etter, T. Irifune, S. Pascarelli, D. F. McMorrow, T. Takayama, H. Takagi, and D. Haskel, Pressure-induced structural dimerization in the hyperhoneycomb iridate β-Li$_2$IrO$_3$ at low temperatures, Phys. Rev. B **100**, 064104 (2019).

[23] M. Seidler, MPMS Analyzer software, https://github.com/miile7/mpms-analyzer.

[24] A. A. Tsirlin, A. O. Zubtsovskii, and E. Uykur, High-resolution x-ray diffraction on decompressed samples of β-Li$_2$IrO$_3$, Eur. Synchrotron Radiat. Facil. (ESRF) (2021).

[25] V. Petříček, M. Dusek, and L. Palatinus, Crystallographic computing system JANA2006: General features, Z. Krist. **229**, 345 (2014).

[26] G. Kresse and J. Furthmüller, Efficiency of *ab-initio* total energy calculations for metals and semiconductors using a plane-wave basis set, Comput. Mater. Sci. **6**, 15 (1996).

[27] G. Kresse and J. Furthmüller, Efficient iterative schemes for *ab initio* total-energy calculations using a plane-wave basis set, Phys. Rev. B **54**, 11169 (1996).

[28] J. P. Perdew, A. Ruzsinszky, G. I. Csonka, O. A. Vydrov, G. E. Scuseria, L. A. Constantin, X. Zhou, and K. Burke, Restoring the Density-Gradient Expansion for Exchange in Solids and Surfaces, Phys. Rev. Lett. **100**, 136406 (2008).

[29] K. Koepernik and H. Eschrig, Full-potential nonorthogonal local-orbital minimum-basis band-structure scheme, Phys. Rev. B **59**, 1743 (1999).

[30] L. S. I. Veiga, M. Etter, K. Glazyrin, F. Sun, C. A. Escanhoela, G. Fabbris, J. R. L. Mardegan, P. S. Malavi, Y. Deng, P. P. Stavropoulos, H.-Y. Kee, W. G. Yang, M. van Veenendaal, J. S. Schilling, T. Takayama, H. Takagi, and D. Haskel, Pressure tuning of bond-directional exchange interactions and magnetic frustration in the hyperhoneycomb iridate β-Li$_2$IrO$_3$, Phys. Rev. B **96**, 140402(R) (2017).

[31] D. Andreica, N. Cavadini, H. U. Güdel, F. N. Gygax, K. Krämer, M. Pinkpank, and A. Schenck, Muon-induced break up of spin-singlet pairs in the double-chain compound KCuCl$_3$, Phys. B: Condens. Matter **289**, 176 (2000).

[32] N. Cavadini, D. Andreica, F. N. Gygax, A. Schenck, K. Krämer, H.-U. Güdel, H. Mutka, and A. Wildes, Local spin susceptibility in KCuCl$_3$, Phys. B: Condens. Matter **335**, 37 (2003).

[33] A. Lappas, A. Schenck, and K. Prassides, Spin-freezing in the two-dimensional spin-gap systems SrCu$_{2-x}$Mg$_x$(BO$_3$)$_2$ ($x = 0$, 0.04, 0.12), Phys. B: Condens. Matter **326**, 431 (2003).

[34] A. Ruiz, V. Nagarajan, M. Vranas, G. Lopez, G. T. McCandless, I. Kimchi, J. Y. Chan, N. P. Breznay, A. Frañó, B. A. Frandsen, and J. G. Analytis, High-temperature magnetic anomaly in the Kitaev hyperhoneycomb compound β-Li$_2$IrO$_3$, Phys. Rev. B **101**, 075112 (2020).

[35] V. N. Antonov, S. Uba, and L. Uba, Electronic structure and x-ray magnetic circular dichroism in the hyperhoneycomb iridate β-Li$_2$IrO$_3$, Phys. Rev. B **98**, 245113 (2018).

[36] V. N. Antonov, D. A. Kukusta, L. Uba, A. Bonda, and S. Uba, Resonant inelastic x-ray scattering spectra in the hyperhoneycomb iridate β-Li$_2$IrO$_3$: First-principles calculations, Phys. Rev. B **103**, 235127 (2021).

[37] J. G. Rau, E. K.-H. Lee, and H.-Y. Kee, Generic Spin Model for the Honeycomb Iridates Beyond the Kitaev Limit, Phys. Rev. Lett. **112**, 077204 (2014).

[38] S. M. Winter, Y. Li, H. O. Jeschke, and R. Valentí, Challenges in design of Kitaev materials: Magnetic interactions from competing energy scales, Phys. Rev. B **93**, 214431 (2016).

[39] M. Majumder, M. Prinz-Zwick, S. Reschke, A. Zubtsovskii, T. Dey, F. Freund, N. Büttgen, A. Jesche, I. Kézsmárki, A. A. Tsirlin, and P. Gegenwart, Field evolution of low-energy excitations in the hyperhoneycomb magnet β-Li$_2$IrO$_3$, Phys. Rev. B **101**, 214417 (2020).

[40] I. Rousochatzakis and N. B. Perkins, Magnetic field induced evolution of intertwined orders in the Kitaev magnet β-Li$_2$IrO$_3$, Phys. Rev. B **97**, 174423 (2018).